Revista Mexicana de Astronomía y Astrofísica, **53**, 79–93 (2017)

A SUBMILLIMETER STUDY OF THE IR DUST BUBBLE S 21 AND ITS ENVIRONS

C. E. Cappa,[1,2] N. U. Duronea,[1] J. Vasquez,[1,2] M. Rubio,[3] V. Firpo,[4,5] C.-H. López-Caraballo,[6] and J. Borissova[7,8]

Received August 3 2016; accepted November 4 2016

RESUMEN

Basados en la emisión molecular en las líneas ^{12}CO(2-1) y ^{13}CO(2-1), y en la emisión en el continuo en el mediano y lejano infrarrojo hacia la burbuja S 21, analizamos las características físicas del gas y polvo asociado con S 21 y la presencia de objetos estelares jóvenes (YSOs) en su entorno. La emisión molecular revela una cáscara grumosa de 1.4 pc de radio rodeando a S 21. Su masa molecular es de 2900 $M_\odot$ y la densidad ambiental original en la región, 2.1×10^3 cm^{-3}, lo que indica que la burbuja evoluciona en un medio de alta densidad. La imagen a 24 μm muestra polvo tibio dentro de la burbuja, mientras que la emisión en el rango 250 a 870 μm revela que hay polvo frío en la vecindad, coincidente con el gas molecular. La detección de emisión en el continuo de radio indica que S 21 es una región HII compacta. Una búsqueda de YSOs utilizando criterios fotométricos permitió identificar muchos candidatos coincidentes con los grumos moleculares. Se analiza si el proceso de *collect and collapse* ha dado origen a una nueva generación de estrellas.

ABSTRACT

Based on the molecular emission in the ^{12}CO(2-1) and ^{13}CO(2-1) lines, and on the continuum emission in the MIR and FIR towards the S 21 IR dust bubble, we analyze the physical characteristics of the gas and dust linked to the nebula and the presence of young stellar objects (YSOs) in its environs. The line emission reveals a clumpy molecular shell, 1.4 pc in radius, encircling S 21. The total molecular mass in the shell amounts to 2900 $M_\odot$ and the original ambient density, 2.1×10^3 cm^{-3}, indicating that the bubble is evolving in a high density interstellar medium. The image at 24 μm shows warm dust inside the bubble, while the emission in the range 250 to 870 μm reveals cold dust in its outskirts, coincident with the molecular gas. The detection of radio continuum emission indicates that the bubble is a compact HII region. A search for YSOs using photometric criteria allowed to identify many candidates projected onto the molecular clumps. We analize if the *collect and collapse* process has triggered a new generation of stars.

Key Words: HII regions — ISM: individual objects (S 21) — ISM: molecules — stars: protostars

1. INTRODUCTION

Massive (O and B-type) stars have an enormous impact on their surroundings due to their ultraviolet (UV) ionizing radiation and energetic winds. Ionized gas in HII regions produces strong infrared (IR), optical, and thermal radio continuum emission. In addition, ionized gas mixed with heated dust makes an HII region bright in thermal IR emission.

[1]Instituto Argentino de Radioastronomía, CONICET, Argentina.
[2]Facultad de Ciencias Astronómicas y Geofísicas, Universidad Nacional de La Plata, Argentina.
[3]Departamento de Astronomía, Universidad de Chile, Chile.
[4]Gemini-CONICYT, Departamento de Física y Astronomía, Universidad de La Serena, La Serena, Chile.
[5]Gemini Observatory, Southern Operations Center, La Serena, Chile.
[6]Universidad Católica de Chile, Santiago, Chile.
[7]Instituto de Física y Astronomía, Universidad de Valparaíso, Chile.
[8]Millennium Institute of Astrophysics (MAS), Santiago, Chile.

A common spatial shape reported for individual Galactic HII regions at IR wavelengths is the ring morphology, or "bubble" seen in projection. A visual examination of the images at 8.0 μm from the Galactic Legacy Infrared Survey Extraordinaire (GLIMPSE; Benjamin et al. 2003) allowed the identification of about 600 full or partial IR dust bubbles (IRDBs) in the inner Galactic plane (Churchwell et al. 2006, 2007) between longitudes from –60° to +60°. Presently, more than 5000 IRDBs have been identified (Simpson et al. 2012). The main characteristics of many of these bubbles were investigated by several authors (see for example Deharveng et al. 2010; Alexander et al. 2013). These bubbles are about 1′ - 3′ in size, show filamentary appearence, and many of them lie close to massive stars and coincide (or enclose) classical and ultracompact HII regions.

At 8 μm, most of the emission originates in strong features of polycyclic aromatic hydrocarbons (PAH) molecules, which are considered to be good tracers of warm UV-irradiated photodissociation regions (PDR; Hollenbach & Tielens 1997). Since these complex molecules are destroyed in the ionized gas (Povich et al. 2007; Lebouteiller et al. 2007), they delineate the ionization front and indicate the presence of substantial amounts of molecular gas surrounding the bubbles. Therefore, these bubbles provide a good insight of the sculpting influences of the UV photons of massive stars on the molecular clouds where they are born.

The geometry of the IR bubbles is also important for understanding triggered star formation scenarios. Classical models, like the *collect and collapse* mechanism (C&C; Elmegreen & Lada 1977) and the *radiative driven implosion* process (RDI; Lefloch & Lazareff 1994), suggest that the formation of stars can be triggered by the action of HII regions over their parental molecular environment. Molecular condensations lying at the border of many galactic bubble-shaped HII regions are then among the most likely sites for stellar births and for early stages of star formation (e.g. Deharveng et al. 2008; Zavagno et al. 2010; Brand et al. 2011; Samal et al. 2014). Detailed studies of IR bubbles have shown the presence of young stellar objects (YSOs) in their environments, although the triggered formation scenario cannot always be proven (e.g. Dewangan & Ojha 2013; Alexander et al. 2013).

As part of a project aimed to study and characterize galactic bubbles, we have selected S 21 from the sample of bubbles reported by Churchwell et al. (2006) to perform a study of its molecular and dust environment, and to search for candidates to YSOs in their vecinity. S 21 is located 10′ east from S 24 (Cappa et al. 2016).

Fig. 1. Composite IRAC image of S 21. The emission at 3.6 μm is in blue, at 4.5 μm is in green, and at 8.0 μm is in red. The positions of IRAS 16495-4418, G341.3553-00.2885, and the catalogued B3-star are indicated with white, yellow, and green crosses, respectively. The color figure can be viewed online.

S 21 is an almost complete circular bubble (see Figure 1) of $\approx$ 0.′75 in radius centered on RA, Dec.(J2000) = $16^h53^m7.9^s$, $-44°23'13.''1$. The dusty nebula appears filamentary at 8 μm, with a rather steep inner border and a more diffuse outer one (Figure 1). The point source IRAS 16495-4418 (RA, Dec.(J2000) = $16^h53^m8.5^s$, $-44°23'21''$) coincides with the bubble. Watson et al. (2010) determined the dust temperature inside the bubble using the emission at 24 and 70 μm from Spitzer-MIPS and a modified blackbody. They found a temperature gradient with the highest temperatures (85 K) close to the center of the bubble and the lowest ones (71 K) close to the border.

Figure 1 reveals a bright point source detected in the IRAC bands, named G341.3553-00.2885 (RA, Dec.(J2000) = $16^h53^m7.12^s$, $-44°23'24.''1$), located close to the center of the bubble. It has counterparts in several optical (GSC, NOMAD, and DENIS) and IR catalogues (2MASS, Spitzer, WISE). Projected close to the northern border of the bubble, the B3-type star HD 329056 (Simbad, $16^h53^m7.63^s$, $-44°22'9.''28$) has been identified.

The distance to S 21 is matter of some debate. Adopting a mean velocity of -44 km s^{-1} for the gas linked to S 21 (see § 3.1), circular galactic rotation

models predict near and far kinematical distances of 3.7 and 12-13 kpc (e.g. Brand & Blitz 1993). Bearing in mind that most of the IRDBs are closer than 8 kpc (Churchwell et al. 2006), we will adopt for S 21 the near kinematical distance of 3.7 kpc. A distance uncertainty of 0.5 kpc results after taking into account a velocity dispersion of 6 km s^{-1} for the interstellar gas.

In this study, we present a molecular line and dust continuum analysis toward S 21 and its environs, with the aim of studying the distribution and physical properties (mass, densities, temperature, kinematics, etc.) of the molecular gas and dust associated with the bubble. We based our study on ^{12}CO(2-1) and ^{13}CO(2-1) data obtained with the APEX telescope[9], and complementary archival IR, optical, and radiocontinuum data.

The simple morphology of S21, along with the strong evidence of star formation in its environs (see below), make this object an excellent laboratory for the investigation of possible scenarios of triggered star formation. With that aim, we also analyze the spatial distribution of the YSO candidates in their vicinity and their relation to the bubble, and search for probable exciting stars.

2. DATA

2.1. *Molecular line observations*

The characteristics of the molecular gas were investigated using ^{12}CO(2-1) (at 230.538000 GHz, HPBW = 30″) and ^{13}CO(2-1) (at 220.398677 GHz, HPBW = 28″) line observations obtained in October 2010 with the Atacama Pathfinder Experiment (APEX) 12-m telescope (G'usten et al. 2006) at Llano de Chajnantor, Chile (Project C-086.F-0674B-2010, P. I.: M. Rubio). As front end for the observations, we used the APEX-1 receiver of the Swedish Heterodyne Facility Instrument (SHeFI; Vassilev et al. 2008). The back end for the observations was the eXtended bandwidth Fast Fourier Transform Spectrometer2 (XFFTS2) with a 2.5 GHz bandwidth divided into 4096 channels. Under good weather conditions, this leads to APEX-1 DSB system temperatures of about 150 K.

The region was observed in the position switching mode using the OTF technique with a space between dumps in the scanning direction of 9″. The rms noise of a single spectrum in the OTF mode was 0.35 K. The off-source position free of CO emission was located at RA, Dec.(J2000) = ($16^h36^m40.56^s$, $-42°3'40''.6$). Calibration was performed using Mars and X-TrA sources. Pointing was done twice during observations using X-TrA, o-Ceti and VY-CMa. The intensity calibration had an uncertainty of 10%. The $C^{18}O$(2-1) line at 219.560357 GHz was also observed, although the emission was very low and was not used in the analysis.

The spectra were reduced using the Continuum and Line Analysis Single-dish Software (CLASS) of the Grenoble Image and Line Data Analysis Software (GILDAS) working group[10]. A linear baseline fitting was applied to the data. The observed line intensities were expressed as main-beam brightness temperatures $T_{\rm mb}$, by dividing the antenna temperature $T_{\rm A}$ by the main-beam efficiency $\eta_{\rm mb}$, equal to 0.72. The Astronomical Image Processing System (AIPS) package and CLASS software were used to perform the analysis. The final molecular data were smoothed to 0.3 km s^{-1}, with a final rms noise of 0.2 K.

2.2. *Archival dust continuum data*

2.2.1. *Herschel data*

The archival data come from the Hi-GAL key program (Hi-GAL:*Herschel* Infrared GALactic plane survey, Molinari et al. 2010), OBSIDs: 1342204094 and 1342204095). These data include PACS images at 70 and 160 μm (Poglitsch et al. 2010) and SPIRE images at 250, 350, and 500 μm (Griffin et al. 2010).The data were re-reduced using the *Herschel* Interactive Processing Environment (HIPE v12[11], Ott 2010) as described in Cappa et al. (2016). The angular resolutions of the final dust continuum images spanned from 8″ to 35.″2 for 70 μm to 500 μm, respectively.

2.3. *Complementary data*

We used archival images of ATLASGAL at 870 μm (345 GHz) (Schuller et al. 2009). This survey has an rms noise in the range 0.05 - 0.07 Jy $beam^{-1}$. The calibration uncertainty in the final maps was about of 15%. The *Large APEX BOlometer CAmera* (LABOCA) used for these observations, was a 295-pixel bolometer array developed by the Max-Planck-Institut fur Radioastronomie (Siringo et al. 2007). The beam size at 870 μm was 19.″2.

[9]APEX, the Atacama Pathfinder EXperiment, is a collaboration between Max Planck Institut fur Radioastronomie (MPIfR), Onsala Space Observatory (OSO), and the European Southern Observatory (ESO).

[10]`http://www.iram.fr/IRAMFR/PDB/class/class.html`

[11]*HIPE* is a joint development by the Herschel Science Ground Segment Consortium, consisting of ESA, the NASA Herschel Science Center, and the HIFI, PACS and SPIRE consortia members, see `http://herschel.esac.esa.int/HerschelPeople.shtml`.

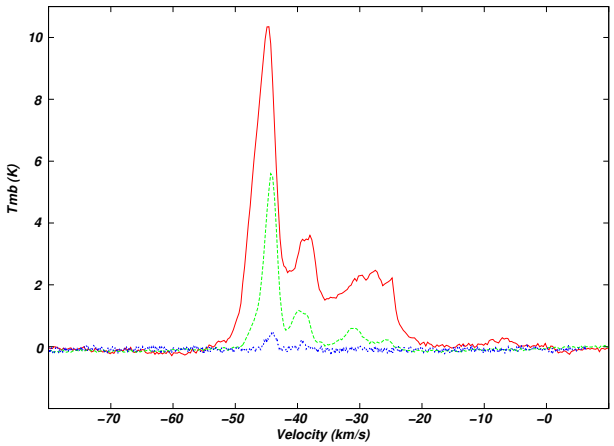

Fig. 2. ^{12}CO(2-1) (red line), ^{13}CO(2-1) (green line), and C^{18}O(2-1) (blue line) averaged molecular line spectra obtained toward S 21. The color figure can be viewed online.

Also, Spitzer images at 3.6, 4.5, and 8.0 μm from the Galactic Legacy Infrared Mid-Plane Survey Extraordinaire (GLIMPSE; Benjamin et al. 2003), and at 24 μm from the MIPS Inner Galactic Plane Survey (MIPSGAL; Carey et al. 2005) were used.

Radio continuum data from the Sydney University Molonglo Sky Survey (SUMSS[12], Bock et al. 1999) at 843 MHz with a resolution of $43'' \times 43''$ csc(Decl.) and an rms noise level of 1 mJy beam^{-1} and at 1.4 GHz from the Southern Galactic Plane Survey (beam size = 1.′7, Haverkorn et al. 2006) were used.

2.4. *Search for young stellar objects*

To investigate the existence of candidates to YSOs projected onto the region we used infrared point sources from the Vista Variables in the Via Lactea ESO Public Survey (VVV, ESO programme ID 179.B-2002; Minniti et al. 2010; Saito et al. 2012), and the Spitzer (Fazio et al. 2004) and Wide-field Infrared Survey Explorer (WISE; Wright et al. 2010) point source catalogues.

3. MOLECULAR GAS LINKED TO THE BUBBLE

3.1. *Molecular gas distribution*

In Figure 2 we show the ^{12}CO(2-1), ^{13}CO(2-1), and C^{18}O(2-1) spectra averaged over a region $\approx 4' \times 4'$ around the central position of S 21. The bulk of the molecular emission appears concentrated between -55 km s^{-1} and -20 km s^{-1}, with three components peaking approximately at -45 km s^{-1}, -38 km s^{-1}, and -30 km s^{-1}. The spatial distribution of these components reveals that only the molecular component peaking at -45 km s^{-1} shows a morphological correspondence with S 21. The emission distribution in the velocity interval from -45.8 to -42.6 km s^{-1} shows a bubble fully inmersed in its parental molecular cloud. CO shells have been reported for many other IRDBs (see for example Arce et al. 2011). Figure 3 displays the integrated ^{13}CO(2-1) emission distribution in the mentioned velocity range in contours overlayed onto the emission at 8 μm. A clumpy circular structure coincident with the infrared bubble with a minimum in the emission projected onto its center can be discerned. The mean radius of the molecular shell is 1.′3. The molecular correspondence between the IR emission at 8 μm and the molecular emission within the quoted velocity interval indicates that the shell is the molecular counterpart of the IR bubble, and that they are physically associated.

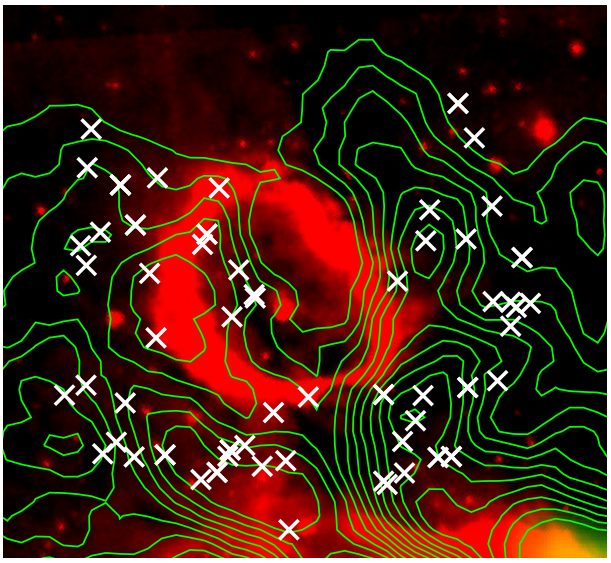

Fig. 3. Overlay of the 8 μm emission (colorscale) and the ^{13}CO emission (in contours) integrated in the velocity range from -45.8 to -42.6 km s^{-1}. Contour levels go from 3 K (≈ 45 *rms*) to 6.9 K in steps of 0.3 K and from 6.9 in steps of 1 K. The white crosses show the position of candidate YSOs identified in the VVV database projected on the molecular shell (see § 7). The color figure can be viewed online.

Using CLUMPFIND we have identified several condensations in the molecular structure around S 21, which will be referred as "clumps" (Blitz 1993; Williams et al. 2000). The location of the clumps,

[12] http://www.astrop.physics.usyd.edu.au/cgi-bin/postage.pl

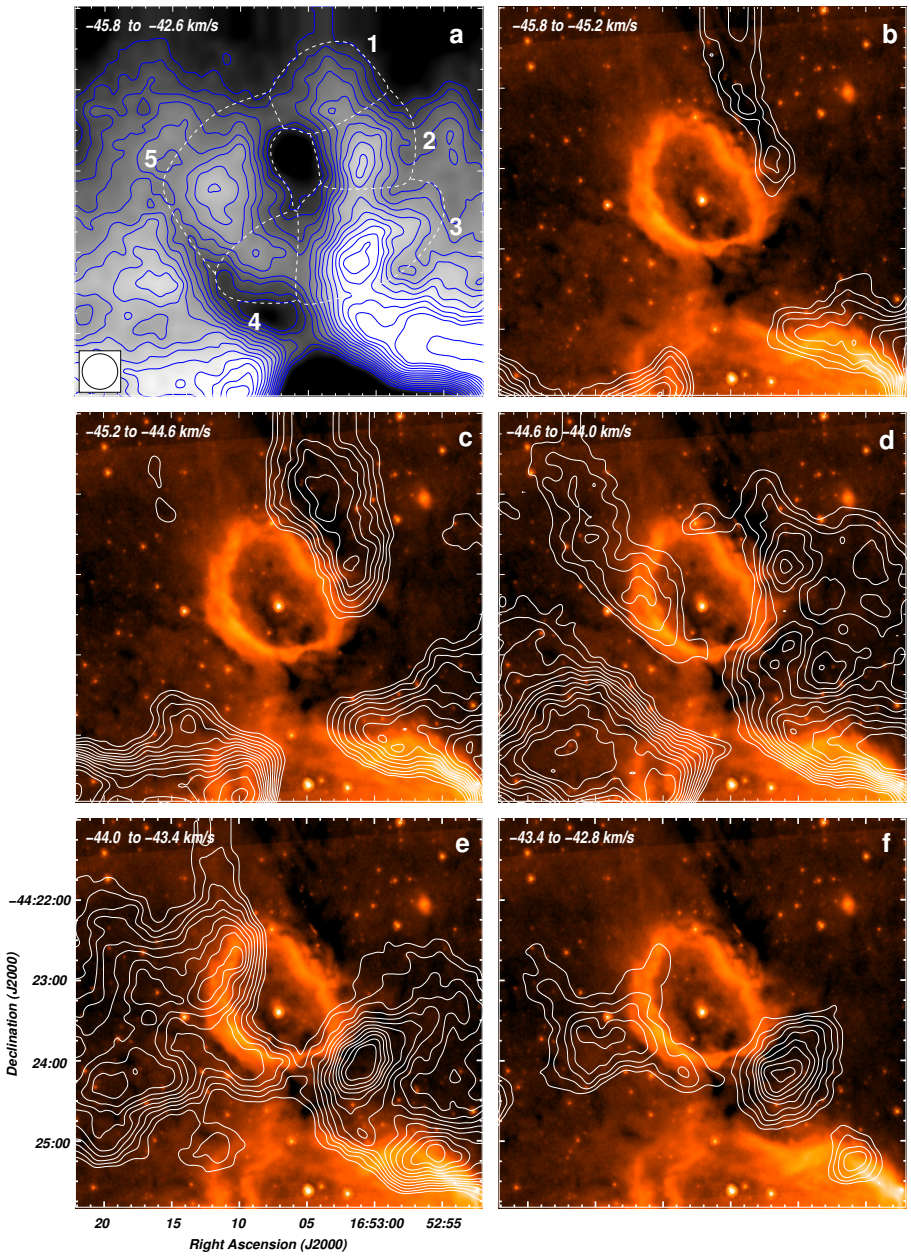

Fig. 4. *Panel a*: ^{13}CO emission in the velocity range from −45.8 to −42.6 km s^{-1}. Contour levels go from 3 K (≈ 45 *rms*) to 6.9 K in steps of 0.3 K and from 6.9 K in steps of 1 K. White dotted lines indicate the limits chosen to define the clumps (see text). The beam size is indicated in the lower left corner of this panel. *Panels b to f*: Channel maps of ^{13}CO in intervals of 0.6 km s^{-1} (white contours) superimposed on the GLIMPSE 8.0 μm red colorscale. Contours go from 4.5 K (≈ 32 K *rms*) to 10 K in steps of 0.5 K, and from 10 K in steps of 1 K. The color figure can be viewed online.

labeled from 1 to 5, is depicted in Figure 4a. We were left only with clumps adjacent to the bubble, which were very likely formed in the collected layers of the molecular gas. The coordinates and peak temperatures of the clumps are listed in Table 1.

In order to unambiguously ascertain the relationship of each clump with the nebula and to provide a better visual display, in Panels *b* to *f* of Figure 4 we show the channel maps of ^{13}CO(2-1) in velocity intervals of 0.6 km s^{-1}, overlaid on the GLIMPSE 8.0 μm emission image. Between −45.8 to −45.2 km s^{-1} (Figure 4b) Clumps 1 and 2 become noticeable, bordering the bubble from its northwestern side. In this velocity range, two bright

TABLE 1

PARAMETERS OF THE MOLECULAR CLUMPS

Clump	R.A.(J2000) (h m s)	Decl.(J2000) (° ′ ″)	T^{12}_{peak} (K)	Δv^{12} (km s^{-1})	T^{13}_{peak} (K)	Δv^{13} (km s^{-1})	$T_{\rm exc}$ (K)	τ^{13}	τ^{12}
1	16:53:03	−44:22:16.3	11.5	3.6	7.5	1.6	16.6	0.96	34.3
2	16:53:00	−44:22:57.3	8.5	2.5	7.3	2.1	13.5	1.83	79.5
3	16:53:01	−44:22:09.2	13.0	4.3	10.2	1.7	18.1	1.50	33.5
4	16:53:08	−44:22:01.3	8.8	3.8	6.5	1.8	13.1	1.28	33.3
5	16:53:12	−44:23:13.7	10.5	4.0	7.8	1.9	15.6	1.30	33.1

TABLE 2

PROPERTIES DERIVED FOR THE MOLECULAR CLUMPS

Clump	Δv (km s^{-1})	$T^{13}_{\rm mean-mb}$ (K)	$\Delta v T^{13}_{\rm mean-mb}$ (K km s^{-1})	$N(^{13}{\rm CO})$ (10^{16} cm^{-2})	R_{eff} (pc)	$M({\rm H_2})$ ($M_\odot$)	n_{H2} (10^3 cm^{-3})	M_{VIR} ($M_\odot$)	$\frac{M_{VIR}}{M({\rm H_2})}$
1	5.0	3.75	12.0	2.4	0.65	350±105	4.6	209-316	0.5-1.3
2	5.4	4.52	14.4	4.0	0.68	650±195	7.5	377-519	0.4-1.1
3	3.7	5.25	16.8	4.2	0.77	880±260	7.0	280-422	0.2-0.7
4	4.8	3.85	12.3	2.8	0.64	400±120	5.5	261-393	0.3-1.4
5	4.6	4.39	14.0	3.2	0.75	620±185	5.3	341-514	0.4-1.2

molecular features can be also detected to the south of S 21, unconnected to this bubble. Clumps 1 and 2 achieve their maximum brightness temperature in the velocity interval from −45.2 to −44.6 km s^{-1} (Figure 4c). Clump 2 is still detected between −44.6 to −44.0 km s^{-1} (Figure 4d), where Clump 3 becomes first noticeable. In this velocity interval, Clump 5 appears as an extension of an elongated feature that borders the eastern side of S 21. From −44.0 to −43.4 km s^{-1} (Figure 4e) Clumps 3, 4, and 5 attain their peak temperature. They surround the nebula from south to east (Clump 3) and from south to north (Clumps 4 and 5). Finally, between −43.4 to −42.8 km s^{-1} (Figure 4f), Clumps 4 and 5 are barely detected but Clump 3 is very bright. Clump 3 dissapears at ≈ −42.1 km s^{-1} (not shown here). At a distance of 3.7 kpc, the radius of the molecular shell is ≈ 1.4 pc.

The eastern section of the molecular shell (Clumps 4 and 5) coincides with the photodissociation region (PDR), while the western section (Clumps 1, 2, and 3) is projected onto regions of low emission at 8 μm close to the PDR.

3.2. *Physical parameters of the molecular gas*

We have estimated some properties for the identified clumps, which are presented in Tables 1 and 2. Assuming that all rotational levels are thermalized with the same excitation temperature (LTE conditions) and that the emission in the ^{12}CO(2-1) line is optically thick, we derived the excitation temperature $T_{\rm exc}$ (Column 8, Table 1) from the emission in the ^{12}CO(2-1) line using

$$T^{12}_{\rm peak} = T^*_{12}\left[\left(e^{\frac{T^*_{12}}{T_{\rm exc}}}-1\right)^{-1}-\left(e^{\frac{T^*_{12}}{T_{\rm bg}}}-1\right)^{-1}\right], \quad (1)$$

where $T^*_{12} = h\nu_{12}/k$, and ν_{12} is the frequency of the ^{12}CO(2-1) line, and $T_{\rm bg} = 2.7$ K. To obtain the peak main-beam brightness-temperature in the ^{12}CO(2-1) line ($T^{12}_{\rm peak}$) (Column 4, Table 1) we used the spectrum toward the position of maximum emission of the clump.

The optical depth τ^{13} (Column 9, Table 1) was obtained from the ^{13}CO(2-1) line by assuming that the excitation temperature is the same for the ^{12}CO(2-1) and ^{13}CO(2-1) emission lines using the expression:

$$\tau^{13} = -\ln\left[1-\frac{{T_{\rm peak}}^{13}}{T^*_{13}}\left[\left(e^{\frac{T^*_{13}}{T_{\rm exc}}}-1\right)^{-1}-\left(e^{\frac{T^*_{13}}{T_{\rm bg}}}-1\right)^{-1}\right]^{-1}\right], \quad (2)$$

where $T^*_{13} = h\nu_{13}/k$, being ν_{13} the frequency of the ^{13}CO(2-1) line. We also estimated the optical depth

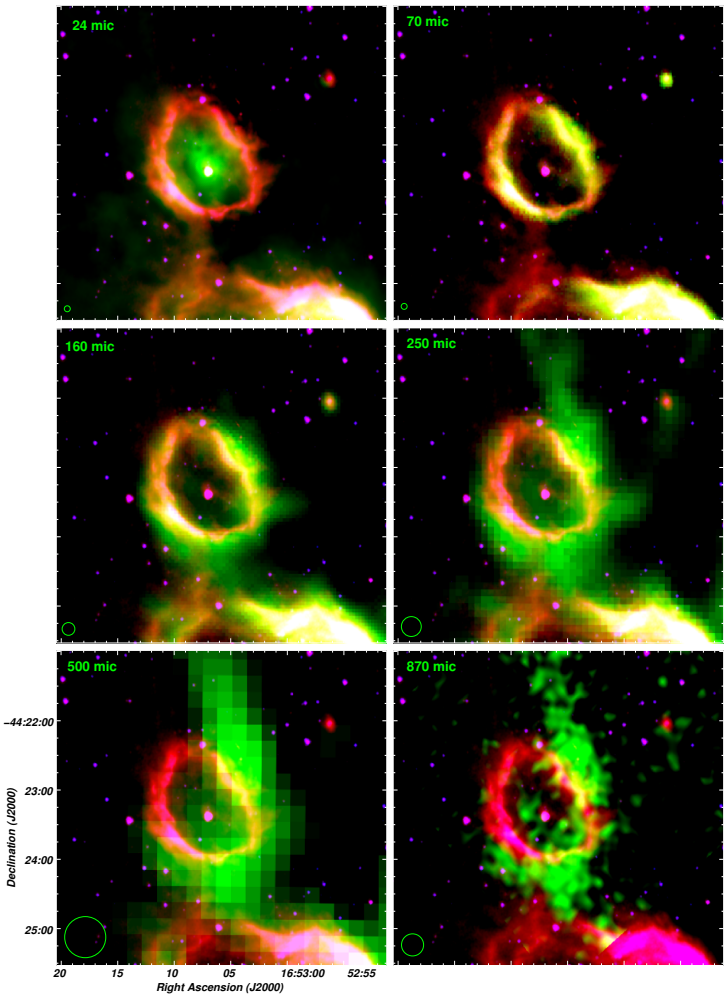

Fig. 5. Composite images showing the emission in the near-, mid-, and far-infrared. All the images display the emissions at 8 μm (in red) and at 3.6 μm (in blue) from IRAC-GLIMPSE. The emissions in green correspond to different IR wavelengths indicated in the upper left corner of each image. The angular resolution of the IR images is shown in the lower left corner. The color figure can be viewed online.

of the ^{12}CO(2-1) line (Column 10, Table 1) from the ^{13}CO(2-1) line with

$$\tau^{12} = \left[\frac{\nu^{13}}{\nu^{12}}\right]^2 \times \left[\frac{\Delta \mathrm{v}^{13}}{\Delta \mathrm{v}^{12}}\right] \times \left[\frac{^{12}\mathrm{CO}}{^{13}\mathrm{CO}}\right] \tau^{13}, \quad (3)$$

where ^{12}CO/^{13}CO is the isotopic ratio (assumed to be $\approx$ 62; Langer & Penzias 1993); $\Delta \mathrm{v}^{13}$ and $\Delta \mathrm{v}^{12}$ are the *full widths at half maximum* (FWHM) of the spectra of the ^{13}CO and ^{12}CO lines, respectively. These values are indicated in Columns 5 and 7 of Table 1.

In LTE, the ^{13}CO column density (Column 5, Table 2) can be estimated from the ^{13}CO(2-1) line data following:

$$N(^{13}\mathrm{CO}) = 2.4\times10^{14}\left[\frac{e^{\frac{T^*_{13}}{T_{\rm exc}}}}{1-e^{-\frac{T^*_{13}}{T_{\rm exc}}}}\right] T_{\rm exc} \int \tau^{13} dv (\mathrm{cm}^{-2}). \quad (4)$$

The integral of Eq. 4 can be approximated by

$$T_{exc} \int \tau^{13} dv \approx \frac{\tau^{13}}{1-e^{(-\tau^{13})}} \int T_{\rm mb} \ \ \mathrm{dv}. \quad (5)$$

This approximation helps to eliminate to some extent optical depth effects and is good within 15% for $\tau < 2$ (Rohlfs & Wilson 2004). Considering that $\tau^{13} < 2$ for the clumps, this approximation is appropriate for our region. The integral was evaluated as

$\Delta v T_{\rm mean-mb}$ (with $T_{\rm mean-mb}$ equal to the average $T_{\rm mb}$ within the area of the clump) and is listed in Column 4, Table 2. Then, the total hydrogen mass (Column 7, Table 2) can be calculated using:

$$M(H_2) \; = \; (m_{\rm sun})^{-1} \; \mu \; m_H \; A \; N(H_2) \; d^2 \qquad (M_\odot), \tag{6}$$

where $m_{\rm sun}$ is the solar mass ($\approx 2\times10^{33}$ g), μ is the mean molecular weight, which is assumed to be equal to 2.76 after allowing for a relative helium abundance of 25% by mass (Allen 1973), m_H is the hydrogen atom mass ($\approx 1.67\times10^{-24}$ g), A is the solid angle of the ^{13}CO emission (included in Table 2 as the effective radius $R_{eff} = \sqrt{A/\pi}$, Column 6), and d is the adopted distance expressed in cm. To obtain the masses, we adopted an abundance $N(H_2)$ / $N(^{13}CO) = 5\times10^5$ (Dickman 1978). Uncertainties in the molecular masses are about 30%, while they are about 50% in the ambient densities, and originate mainly from the distance uncertainties.

Mean volume densities of the clumps are in the range (4.5-7)$\times10^3$ cm^{-3} (Column 8 of Table 2). We estimate the original mean volume ambient density in the region of the bubble by assuming a uniform gas distribution before the ring was formed. This density was obtained by distributing the total shell mass within a sphere with the outer radius of the shell (1.7 pc), and amounts to 2.1×10^3 cm^{-3}. This value indicates that the bubble is evolving in a high density interstellar medium.

4. THE INTERSTELLAR DUST LINKED TO THE BUBBLE

4.1. *Dust distribution*

Dust associated with the bubble can be analyzed from the distribution of the emission at different wavelengths in the infrared.

Each panel of Figure 5 shows a composite image of the emissions at 8 μm (in red) and 3.6 μm (in blue) from IRAC-GLIMPSE, and the emissions at 24, 70, 160, 250, 500, and 870 μm (in green) from MIPS, *Herschel*-PACS and -SPIRE, and ATLASGAL.

The emission at 24 μm is seen projected onto the inner part of the bubble, with its maximum near the central point source. The emission at 70 μm coincides fairly well with that at 8 μm. The emission differs significantly at larger wavelengths. At 160 μm it encircles externally the bubble completely and appears more extended than at 70 μm. At 250 and 500 μm, the emission is brighter than at lower wavelengths and extends toward the western and northern parts of the bubble. The SPIRE emission distribution at 350 μm (not shown here) is similar to that at 250 and 500 μm. Similarly to the case of S 24, cold dust emission detected at 870 μm resembles that at 250 and 500 μm, although the emission at 250 and 500 μm, which also shows the distribution of cold dust, appears more extended. We have to bear in mind that large scale dust continuum emission might be filtered out in LABOCA bolometric observations.

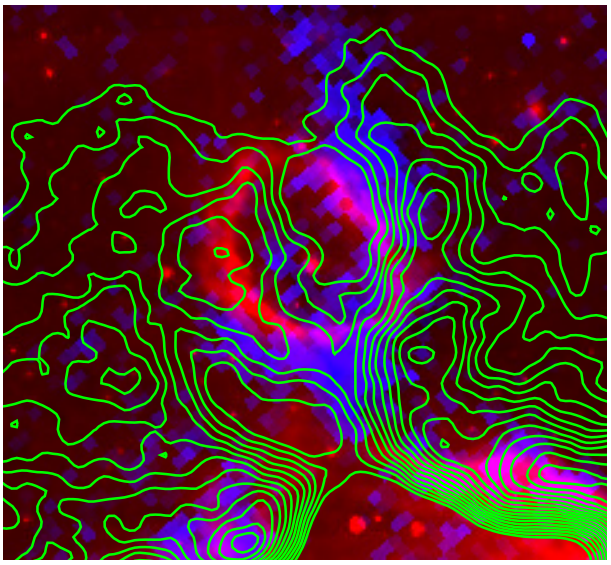

Fig. 6. Composite image showing the emission at 8 μm (in red) and at 870 μm (in blue), and the same ^{13}CO contours of Figure 3. The color figure can be viewed online.

Two facts can be concluded from these images. On the one hand the spatial emission distribution in the mid- and far-IR seems to show a gradient in dust temperature, with lower values in the outer regions of the bubble where continuum emission at larger wavelengths dominates. Indeed, emission at $\lambda > 160\mu$m is present well outside the PDR. On the other hand, the emission at 24 μm inside S 21 is indicative of the presence of exciting sources. Both statements will be analyzed in some detail in the next sections.

A comparison with the molecular gas distribution around the bubble (see Figure 6) shows that Clumps 1 to 4 partially coincide with the cold dust counterpart identified in the *Herschel*-SPIRE and in the LABOCA images.

The observed dust continuum emission at different wavelengths in the IR coincides with previous findings toward other IR dust bubbles.

The molecular emission from the ^{12}CO(2-1) line may contribute to the thermal emission at 870 μm. In our case, this contribution is less than about 1%

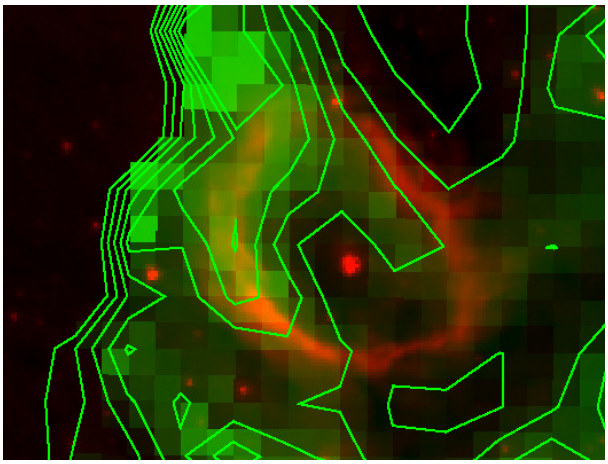

Fig. 7. Dust temperature map derived from the Herschel emission at 250 and 350 μm superimposed on the image at 8 μm. Blue color scale goes from 15 to 33 K. Brighter blue regions indicate higher dust temperatures. Contour levels correspond to 15 to 30 K, in steps of 3 K. The color figure can be viewed online.

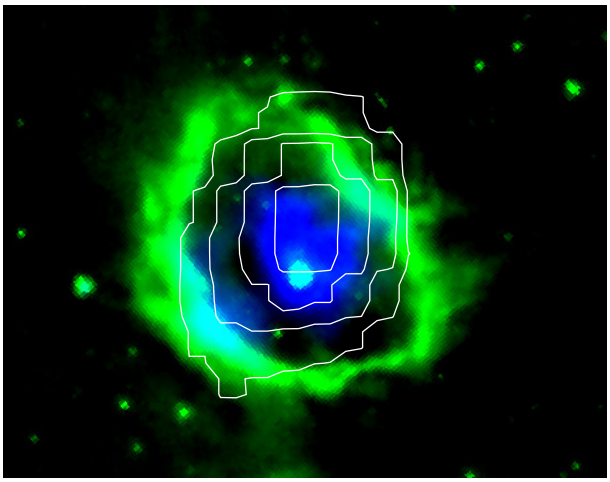

Fig. 8. Overlay of the radio continuum emission at 843 MHz (white contours), the IRAC emission at 8μm (in green), and the MIPSGAL emission at 24μm (in blue). Contours correspond to 10, 15, 20, and 25 mJy beam^{-1}. The color figure can be viewed online.

of the emission at 870 μm, and consequently, within the calibration uncertainties. The other process that contributes to the emission at 870 μm is the free-free emission from ionized gas. This contribution, bearing in mind the flux density at 1.4 GHz (see § 5), is less than 0.1% of the emission at 870 μm, and again, within the calibration uncertainties.

4.2. *Dust temperatures and mass*

Dust temperatures T_{dust} in the environs of the S 21 region can be obtained using the SPIRE images at 250 μm and 350 μm. To perform this we convolved the image at 250 μm down to the angular resolution at 350 μm and assumed that the emission is optically thin. The *color-temperature* map was constructed as the inverse function of the ratio map of Herschel 250 μm and 350 μm color-and-background-corrected maps, i.e., $T_{dust} = f(T)^{-1}$, where $f(T)$ is:

$$f(T) = \frac{S_{250}}{S_{350}} = \frac{B_\nu(250\,\mu m, T)}{B_\nu(350\,\mu m, T)} \left(\frac{250}{350}\right)^{\beta_d} \qquad (7)$$

In this expresion S_{250} and S_{350} are the flux densities in Jy beam^{-1}, $B_\nu(\nu, T)$ is the blackbody Planck function and β_d, the spectral index of the thermal dust emission. The pixel-to-pixel temperature was calculated assuming $\beta_d = 2$. This is a typical value adopted for irradiated regions.

The dust temperature map is shown in Figure 7. The highest dust temperatures (33 K) are present at the NE extreme of the 8 μm bubble. Values in the range 24-33 K coincide with the eastern section of the bubble, while lower values (21 K) are obtained for the western side. Low dust temperatures coincide with molecular gas and with regions with faint emission at 8 μm. Watson et al. (2010) derived dust temperatures for the interior of S 21 based on images from MIPS at 24 μm (whose emission is detected inside the bubble) and 70 μm (detected up to the border of the bubble). Our estimates, based on images in the far IR, sample colder dust present in the outkirts of the bubble.

Dust masses can be estimated from the expression (Hildebrand 1983):

$$M_{dust} = \frac{S_{870}\ d^2}{\kappa_{870}\ B_{870}(T_{dust})} \qquad (8)$$

where S_{870} is the flux density at 870 μm, $d = 3.7 \pm 0.5$ kpc, $\kappa_{870} = 1.0$ cm^2/gr is the dust opacity per unit mass (Ossenkopf & Henning 1994), and $B_{870}(T_{dust})$ is the Planck function for a temperature T_{dust}.

The flux density S_{870} obtained by integrating the emission over the observed emitting area linked to S 21 at this wavelength (see Figure 5f) amounts to 1.9±0.4 Jy. Adopting a mean value $T_{dust} = 30$ K for S 21, a dust mass $M_{dust} = 1.53$±0.90 $M_\odot$ can be estimated. For gas-to-dust ratios in the range 100-186 (Beuther et al. 2011), the gas mass amounts to 153-285 $M_\odot$.

5. THE IONIZED GAS

Figure 8 shows an overlay of the SUMSS image at 843 MHz (in white contours) and the emissions at 8 μm and 24 μm (in colorscale). The 843 MHz image (synthesized beam = $43''\times62''$) shows a radio source coincident with S 21 catalogued by Murphy et al. (2007) with a size of $75\farcs7\times69\farcs6$ and a flux density $S_{0.843} = 49.2$ mJy. The elongated shape of the source is due to the synthesized beam of the data. The source is also detected at 1.4 GHz (SGPS, Haverkorn et al. 2006) with an estimated flux density of $S_{1.4} = 52$ mJy. With these values, the derived spectral index $\alpha \simeq +0.1$ ($S_\nu \propto \nu^\alpha$). Within uncertainties, this value is consistent with thermal emission of an HII region optically thick at 843 MHz.

Thus, these results indicate the presence of ionized gas, and consequently, the existence of at least one exciting source, compatible with warm dust inside the bubble as shown by the 24 μm image. The emission at 8 μm due to PAHs reveals a PDR bordering the ionized region and the presence of molecular gas in its exterior. The radius of the ionized region inside the 8 μm dust bubble is $38''$ or 0.7 pc at 3.7 kpc. The derived spectral index confirms the classification of S 21 as an HII region by Anderson et al. (2015). The characteristics of the region, visible in the IR and in the radio continuum, as well as the large mean original ambient density of 2100 cm^{-3} (see § 3.2) suggest a compact HII region (Urquhart et al. 2013).

To produce the observed flux at 1.4 GHz we require an UV photon flux that can be obtained from Matsakis et al. (1976)

$$N_{Ly} = 7.5\times10^{43} S_{1.4}\nu^{0.1} d^2 T_e^{-0.45} \quad s^{-1} \qquad (9)$$

where $S_{1.4}$ is in units of mJy, ν in GHz, d in kpc, and the electron temperature T_e in 10^4 K. Considering the galactic electron temperatures for HII regions (Quireza et al. 2006), we assumed $T_e = 7000$ K. The required UV flux amounts to 6.5×10^{46} s^{-1}. This ionizing flux is underestimated since part of the stellar UV photons are used to heat the dust. Considering that half of the stellar photons are absorbed by dust (Inoue 2001), the UV photon flux would be 1.3×10^{47} s^{-1}. According to Martins et al. (2005), this value indicates that the ionization of the gas could be produced by an O9.5V or earlier type star.

6. SEARCH FOR AN EXCITING STAR

Identifying the exciting star of this HII region is not an easy task. The extinction towards the inner part of the IR bubble can help to identity this star since we expect for it a similar extinction. This extinction can be deduced from the expresion by Bohlin et al. (1978):

$$N(HI) + 2N(H_2) = 5.8\times10^{21} E(B-V) \qquad (10)$$

Considering only the H_2 column density toward the IR source and taking into account $N(H_2) = 2.9\times10^{21}$ cm^{-2} (estimated from the ^{13}CO emission), we calculate a visual absorption of 30 mag.

To search for exciting stars the color-magnitude diagrams were built using the VVV DR4 catalog (Figure 8). The foreground main sequence stars are situated around $J-K_s = 0.7$ mag, and the mean reddening is estimated as $E(J-K_s) = 0.5$ mag; some field red giants can be also identified. The 76 extremely red stars ($(J-K_s) > 4$ mag) are projected in the field (see also the lower panel of Figure 9); seven of them are projected within the inner radius of the bubble and could be candidates for the exciting source. However, all of them are too faint and a spectroscopic follow up is necessary to reveal their nature.

As pointed out in § 1, G341.3553-00.2885, located close to the center of the IR bubble, is detected both in the optical and at IR wavelengths, appearing saturated in the VVV images. The analysis of the emission of this IR source using the VOSA[13] and TLUSTY[14] tools and all the available detections at different wavelengths (taking into account stellar atmosphere models for O and B stars) suggests that the star might be a O8V or a B0I star. From the comparison of the observed colors taken from the 2MASS catalogue (source 2MASSJ 16530711-4423239) with the intrinsic magnitudes and colors taken from Martins & Plez (2006) for O8V stars and from Bibby et al. (2008) for B0I stars, we estimate visual absorptions and distances of 21 mag and 0.58±0.9 kpc for an O8V type star and 20.9 mag and 1.7±0.8 kpc for a B0I type star, using the standard reddening law and Bessel et al. (1998) transformations. The calculated distance is not comparable with the kinematical distance of 3.7 kpc to the complex. Thus, G341.3553-00.2885 is most probably a foreground object. Spectroscopic data are necessary to verify this suggestion and to unambiguously identify the exciting star of this bubble, but this is beyond the scope of this paper.

7. STAR FORMATION TOWARD S 21

As pointed out in § 1, star formation can be favored in the molecular and cold dust clumps in the

[13] http://www.svo2.cab.inta-csic.es/theory/vosa.
[14] http://www.nova.astro.umd.edu

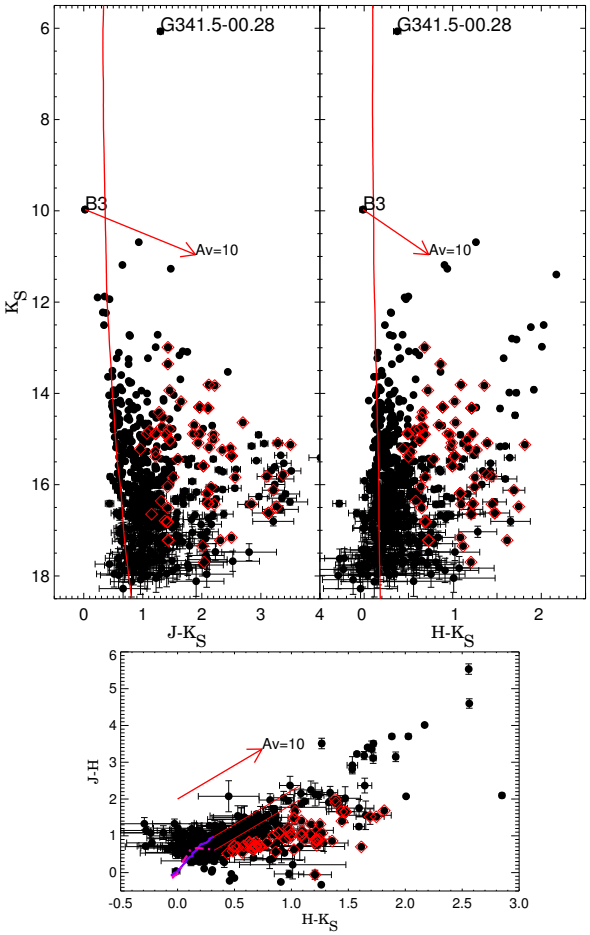

Fig. 9. *Upper panel.* $(J - K_s)$ vs. K_s and $(H - K_s)$ vs. K_s VVV color magnitude diagrams within a radius of 1.′5 centered on S 21. The vertical red line is the zero age main sequence, reddened with $E(J - K_s) = 0.5$ mag (the mean reddening of the field stars). The candidate YSOs projected on the molecular shell are overplotted as red squares. The red arrow shows the reddening vector corresponding to Av=10 mag. The G341.3553-00.2885 and HD 329056 sources are labeled. *Bottom panel.* The $(H - K_s)$ vs. $(J - H)$ color-color diagram. The continuous and dashed lines represent the sequence of the zero-reddening stars of luminosity classes I (Koornneff et al. 1983) and V (Schmidt-Kaler 1982). The color figure can be viewed online.

environs of HII regions. To help testing if this is the case for the S 21 bubble, we can analyze the stability of the molecular clumps by comparing virial to LTE masses. Following MacLaren et al. (1988), the virial mass can be obtained as:

$$\frac{M_{\rm vir}}{M_\odot} = k_2 \left[\frac{R}{\rm pc}\right] \left[\frac{\Delta {\rm V}^2}{\rm km\ s^{-1}}\right] \qquad (11)$$

where R and ΔV are the radius of the region and the velocity width measured from the ^{13}CO(2-1) emission, and k_2 depends on the density distribution in the clump, being 190 or 126 according to $\rho \propto r^{-1}$ or $\rho \propto r^{-2}$, respectively. Virial masses are included in Column 9 of Table 2 for the two density profiles. The ratio $\frac{M_{\rm vir}}{M(H_2)} = \gamma$ is listed in Column 10.

As classical virial equilibrium analysis establishes, a ratio $\gamma > 1$ would imply that the clumps could be stable against collapse, while lower values indicate that collapse is possible. The derived ratio for Clump 3 is consistent with collapse, while results for the other four clumps are not conclusive.

Both virial and LTE masses have large uncertainties due to the distance indetermination (30% for $M(H_2)$ and 15% for M_{VIR}). Minor errors are due to uncertainties in the boundaries of the clumps resulting in errors in their areas and in the LTE masses.

Virial masses are not free of additional errors, since the existence of magnetic fields might overestimate by up to a factor of 2 the derived values (MacLaren et al. 1988). Another source of error is the density profile of the clump, which is unknown. Uncertainties in the distance in the LTE mass and those due to the density profile in virial masses were taken into account in the value of γ.

To investigate if YSOs are detected toward the molecular clumps we performed a search for candidates in the available point source catalogues within a region of 1.′5 centered on the bubble. In the region of the bubble and the surrounding molecular shell, no sources with characteristics of YSOs were identified in the Spitzer and WISE databases by applying color criteria (Allen et al. 2004 for Spitzer data; Koenig et al. 2012 for WISE data), mainly because the WISE data are not deep enough to measure the fainter stars.

To select new candidate YSOs in the region we used the VVV database and applied photometric criteria. First, from the near-infrared $(J - H)/(H - K)$ color - color diagram we selected all stars which were at least 3σ distant from the reddening line that marks the colors of dwarf stars. The list thereby obtained was cross-matched with GLIMPSE measurements. They are shown in Figure 10. The objects with $[K_{\rm S} - [3.6]] > 0.5$ or $[[3.6] - [4.5]] > 0.5$ magnitudes are considered to be most probable Class I and Class II YSOs. These limits are set in order to avoid selecting objects that are more likely Class III objects or normal stars (dashed red line in Figure 10). Our final list contains 71 YSO candidates.

The location of the sources in the color magnitude and color-color diagrams is shown in Figure 9, while Figure 3 shows their spatial correlation with

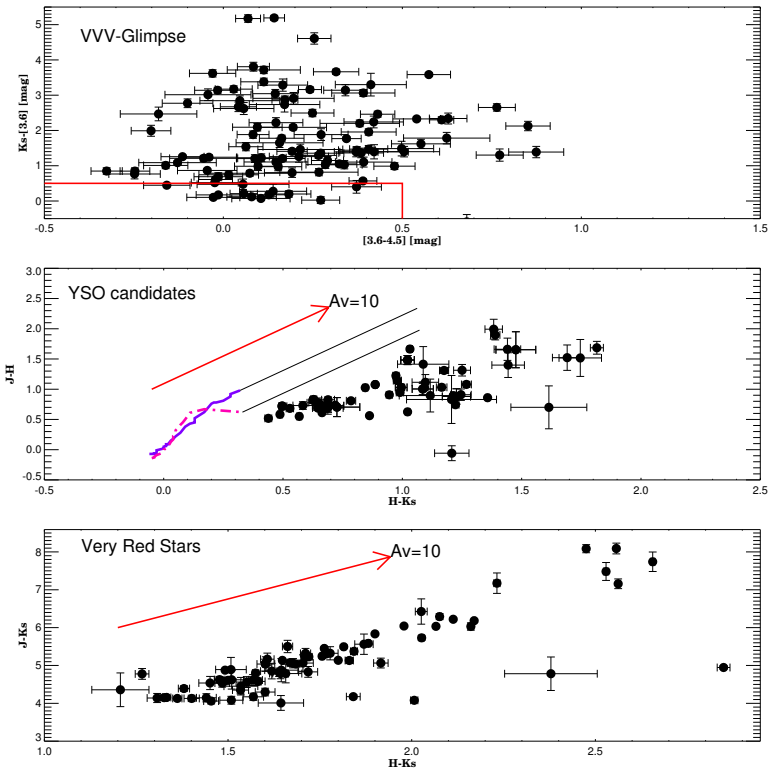

Fig. 10. *Upper panel.* The $K_S - [3.6]$,$[3.6] - [4.5]$ color-color plot of stars that are detected in GLIMPSE I. The red dashed lines represent the limits used to select Class I and Class II YSOs. *Middle panel.* The $(J - H)$ vs. $(H - K_S)$ color-color diagram of the sample. The continuous and dashed lines represent the sequence of the zero-reddening stars of luminosity classes I (Koornneef et al. 1983) and V (Schmidt-Kaler 1982). *Lower panel.* The extremely red stars detected in the field. The color figure can be viewed online.

the molecular clumps. The presence of candidate YSOs projected on the molecular shell suggests that star formation has been active recently. However, it is not possible to determine if all candidate YSOs are linked to the molecular shell around S 21.

The widely known *collect-and-collapse* mechanism (C&C; Elmegreen & Lada 1977) proposes that the expansion of an ionization front over its parental molecular cloud can trigger the star formation process. The molecular gas may fragment alongside the ionization front as it expands and the fragments may become inestable, giving rise to a new generation of stars. To test whether the C&C mechanism has triggered star formation in the molecular shell around S 21 we applied the analytical model by Whitworth et al. (1994). For the case of HII regions, the model predicts the age of the HII region at which the fragmentation occurs (the fragmentation time scale), $t_{\rm frag}$, the size of the HII region at that moment, $R_{\rm frag}$, the mass of the fragments, $M_{\rm frag}$, and their separation along the compressed layer, $r_{\rm frag}$. The parameters required to derive these quantities are the UV photon flux of the exciting star, $N_{\rm Ly}$, the ambient density of the surrounding medium into which the HII region is evolving, n_0, and the isothermal sound speed in the shocked gas, a_s.

To estimate these parameters we took into account a large range of spectral types, i.e. from O3V to O9.5V stars, with UV fluxes in the range $N_{\rm Ly} = (43-0.4)\times10^{48}$ s^{-1} (Martins et al. 2005). Using the mean H_2 ambient density $n_{H2} = 2100$ cm^{-3} (see § 3.2), and a_s = 0.2-0.6 km s^{-1}, we obtained $t_{\rm frag} = (1.0 - 1.5) \times 10^6$ yr, $R_{\rm frag} = 4.3 - 3.0$ pc, $M_{\rm frag}$ = 20-29 $M_\odot$, and, $r_{\rm frag}$ = 0.5-0.3 pc.

The dynamical age of the HII region can be estimated using the equation (Dyson & Williams 1997):

$$t_{\rm dyn} = \frac{4R_S}{7c_s}\left[\left(\frac{R}{R_S}\right)^{7/4} - 1\right] \qquad (12)$$

where R_S is the original Strömgren radius, equal to 0.13-0.63 pc for the adopted spectral types, and c_s is the sound velocity in the ionized gas. Derived dynamical ages span the range $(1.4\text{-}33)\times10^4$ yr.

We found that the dynamical age is significantly smaller than the fragmentation time scale $t_{\rm frag}$ for the adopted ambient density, and hence, the C&C process does not seem to be responsible for the triggering of star formation in the envelope. An RDI scenario could be investigated. However, evidences of this process (such the presence of pillars) appear to be absent. The rest of the parameters, $R_{\rm frag}$, $M_{\rm frag}$, and $r_{\rm frag}$, confirmed that the HII region is too young to start triggering.

8. CONCLUSIONS

We performed a multiwavelength study of the IR dust bubble S 21 using APEX observations of the ^{12}CO(2-1) and ^{13}CO(2-1) lines and complementary images in the near-, mid-, and far-IR from IRAC-Glimpse, MIPSGAL, Herschel, and ATLASGAL.

The molecular emission in the ^{12}CO(2-1) and ^{13}CO(2-1) lines obtained with the APEX telescope toward the IR dust bubble S 21 revealed a molecular shell encircling the bubble and partially coincident with the PDR shown by the IRAC emission at 8 μm. With a mean radius of 1.4 pc, the molecular shell is larger than the 8 μm bubble. This shell is detected in the velocity interval from –45.8 to –42.6 km s^{-1}. The velocity of the shell confirms that S 21 belongs to the same complex than S 24. Five clumps were identified in the molecular shell, with radii in the range 0.64-0.75 pc, LTE masses of 350-880 $M_{\odot}$, and volume densities of (4.5-7)$\times10^3$ cm^{-3}. Virial masses for the clumps suggest that at least one of them can collapse. The original ambient density in the region was about 2100 cm^{-3}.

Complementary images in the near-, mid-, and far-IR from IRAC-Glimpse, Herschel, and ATLASGAL were used to characterize the dust linked to the bubble. The emission at 24 μm coincided with the inner part of the bubble, indicating warm dust inside. The spatial distribution of the emission in the far-IR from 70 to 160 μm coincided with the 8 μm bubble and the molecular emission, while the emission at 500 and 870 μm resembled that at 250 μm. The spatial distribution of the Herschel-PACS and Spire, and ATLASGAL emissions showed a cold dust component coincident with the molecular gas. Dust temperature determinations using the emissions at 250 and 350 μm allowed us to estimate dust temperatures in the range 21-33 K for the cold dust component linked to the 8 μm bubble.

Thermal radio continuum emission at 843 MHz and 1.4 GHz was detected from inside the bubble, indicating the existence of ionized gas and excitation sources, in agreement with the presence of warm dust. We conclude that a compact HII region has developed. However, the identification of the exciting star is a difficult task and deserves additional studies.

A search for candidate YSOs was performed. We were able to identify many candidates in the VVV database projected on the molecular clumps, although it is not clear whether all these candidates are linked to the molecular shell. This result suggests that star formation has been active recently. The HII region is probably very young for the C&C process to be active.

C.E.C. acknowledges the kind hospitality of M. Rubio and her family during her stay in Chile. V.F. acknowledges support from CONICYT Astronomy Program-2015 Research Fellow GEMINI-CONICYT (32RF0002) and from the Faculty of the European Space Astronomy Centre (ESAC), and would like to thank Ivan Valtchanov, Bruno Altieri, and Luca Conversi for their support and valuable assistance in the Herschel data processing. We acknowledge the anonymous referee for very helpful comments. The ATLASGAL project is a collaboration between the Max-Planck-Gesellschaft, the European Southern Observatory (ESO) and the Universidad de Chile. This project was partially financed by CONICET of Argentina under project PIP 0356, UNLP under project 11/G120, and CONICYT of Chile through FONDECYT grant No. 1140839. We gratefully acknowledge the use of data from the ESO Public Survey programme ID 179.B-2002 taken with the VISTA telescope and data products from the Cambridge Astronomical Survey Unit. Support for JB is provided by the Ministry of Economy, Development, and Tourism's Millennium Science Initiative through grant IC120009, awarded to The Millennium Institute of Astrophysics, MAS. This work is based [in part] on observations made with the Spitzer Space Telescope, which was operated by the Jet Propulsion Laboratory, California Institute of Technology under a contract with NASA. This publication makes use of data products from the Two Micron All Sky Survey, which is a joint project of the University of Massa chusetts and the Infrared Processing and Analysis Center/California Institute of Technology, funded by the National Aeronautics and Space Administration and the National Science Foundation.

REFERENCES

Alexander, M. J., Kobulnicky, H. A., Kerton, C. R., & Arvidsson, K. 2013, ApJ, 770, 1

Allen, C. W. 1973, ed. London: University of London, Athlone Press, 3rd ed.

Allen, L. E., Calvet, N., D'Alessio, P., et al. 2004, ApJS, 154, 363
Anderson, L. D., Deharveng, L., Zavagno, A., et al. 2015, ApJ, 800, 101
Arce, H. G., Borkin, M. A., Goodman, A. A., Pineda, J. E., & Beaumont, C. N. 2011, ApJ, 742, 105
Benjamin, R. A., Churchwell, E., Babler, B. L., et al. 2003, PASP, 115, 953
Bessell, M. S., Castelli, F., & Plez, B. 1998, A&A, 333, 231
Beuther, H., Linz, H., Henning, T., et al. 2011, A&A, 531, A26
Bibby, J. L., Crowther, P. A., Furness, J. P., & Clark, J. S. 2008, MNRAS, 386, L23
Blitz, L. 1993, in Protostars and Planets III, ed. E. H. Levy & J. I. Lunine, 125, 161
Bock, D. C.-J., Large, M. I., & Sadler, E. M. 1999, AJ, 117, 1578
Bohlin, R. C., Savage, B. D., & Drake, J. F. 1978, ApJ, 224, 132
Brand, J. & Blitz, L. 1993, A&A, 275, 67
Brand, J., Massi, F., Zavagno, A., Deharveng, L., & Lefloch, B. 2011, A&A, 527, A62
Cappa, C. E., Duronea, N., Firpo, V., et al. 2016, A&A, 585, A30
Carey, S. J., Noriega-Crespo, A., Price, S. D., et al. 2005, in Bulletin of the American Astronomical Society, Vol. 37,American Astronomical Society Meeting Abstracts
Churchwell, E., Povich, M. S., Allen, D., et al. 2006, ApJ, 649, 759
Churchwell, E., Watson, D. F., Povich, M. S., et al. 2007, ApJ, 670, 428
Deharveng, L., Lefloch, B., Kurtz, S., et al. 2008, A&A, 482, 585
Deharveng, L., Schuller, F., Anderson, L. D., et al. 2010, A&A, 523, A6
Dewangan, L. K. & Ojha, D. K. 2013, MNRAS, 429, 1386
Dickman, R. L. 1978, ApJS, 37, 407
Dyson, J. E. & Williams, D. A. 1997, The physics of the interstellar medium, ed. Dyson, J. E. & Williams, D. A.
Elmegreen, B. G. & Lada, C. J. 1977, ApJ, 214, 725
Fazio, G. G., Hora, J. L., Allen, L. E., et al. 2004, ApJS, 154, 10
Griffin, M. J., Abergel, A., Abreu, A., et al. 2010, A&A, 518, L3
Güsten, R., Nyman, L. A., Schilke, P., et al. 2006, A&A, 454, L13
Haverkorn, M., Gaensler, B. M., McClure-Griffiths, N. M., Dickey, J. M., & Green, A. J. 2006, ApJS, 167, 230
Hildebrand, R. H. 1983, QJRAS, 24, 267
Hollenbach, D. J. & Tielens, A. G. G. M. 1997, ARA&A, 35, 179
Inoue, A. K. 2001, AJ, 122, 1788
Koenig, X. P., Leisawitz, D. T., Benford, D. J., et al. 2012, ApJ, 744, 130
Koornneef, J. 1983, A&A, 128, 84
Langer, W. D. & Penzias, A. A. 1993, ApJ, 408, 539
Lebouteiller, V., Brandl, B., Bernard-Salas, J., Devost, D., & Houck, J. R. 2007, ApJ, 665, 390
Lefloch, B. & Lazareff, B. 1994, A&A, 289, 559
MacLaren, I., Richardson, K. M., & Wolfendale, A. W. 1988, ApJ, 333, 821
Martins, F. & Plez, B. 2006, A&A, 457, 637
Martins, F., Schaerer, D., & Hillier, D. J. 2005, A&A, 436, 1049
Matsakis, D. N., Evans, II, N. J., Sato, T., & Zuckerman, B. 1976, AJ, 81, 172
Minniti, D., Lucas, P. W., Emerson, J. P., et al. 2010, New A, 15, 433
Molinari, S., Swinyard, B., Bally, J., et al. 2010, A&A, 518, L100
Murphy, T., Mauch, T., Green, A., et al. 2007, MNRAS, 382, 382
Ossenkopf, V. & Henning, T. 1994, A&A, 291, 943
Ott, S. 2010, in Astronomical Society of the Pacific Conference Series, Vol. 434, Astronomical Data Analysis Software and Systems XIX, ed. Y. Mizumoto, K.-I. Morita, & M. Ohishi, 139
Poglitsch, A., Waelkens, C., Geis, N., et al. 2010, A&A, 518, L2
Povich, M. S., Stone, J. M., Churchwell, E., et al. 2007, ApJ, 660, 346
Quireza, C., Rood, R. T., Bania, T. M., Balser, D. S., & Maciel, W. J. 2006, ApJ, 653, 1226
Rohlfs, K. & Wilson, T. L. 2004, Tools of Radioastronomy , ed. Springer-Verlag, Berlin-Heidelberg
Saito, R. K., Hempel, M., Minniti, D., et al. 2012, A&A, 537, A107
Samal, M. R., Zavagno, A., Deharveng, L., et al. 2014, A&A, 566, A122
Schmidt-Kaler, H., 1982, Landolt-Bornstein, Group IV, Vol. 2, Subvol. b, edited by K. Schaifers and H. H. Voigt (Springer, Verlag)
Schuller, F., Menten, K. M., Contreras, Y., et al. 2009, A&A, 504, 415
Simpson, R. J., Povich, M. S., Kendrew, S., et al. 2012, MNRAS, 424, 2442
Siringo, G., Weiss, A., Kreysa, E., et al. 2007, The Messenger, 129, 2
Urquhart, J.S., Thompson, M.A., Moore, T.J.T., Purcell, C.R., et al. 2013, MNRAS, 435, 400
Vassilev, V., Meledin, D., Lapkin, I., et al. 2008, A&A, 490, 1157
Watson, C., Hanspal, U., & Mengistu, A. 2010, ApJ, 716, 1478
Whitworth, A. P., Bhattal, A. S., Chapman, S. J., Disney, M. J., & Turner, J. A. 1994, MNRAS, 268, 291
Williams, J. P., Blitz, L., & McKee, C. F. 2000, Protostars and Planets IV, 97
Wright, E. L., Eisenhardt, P. R. M., Mainzer, A. K., et al. 2010, AJ, 140, 1868
Zavagno, A., Russeil, D., Motte, F., et al. 2010, A&A, 518, L81

Nicolás U. Duronea, Javier Vasquez and Cristina E. Cappa: Instituto Argentino de Radioastronomía, CONICET, CCT La PLata, C.C.5, 1894, Villa Elisa, Argentina (cristina.elisabet.cappa@gmail.com).
Javier Vasquez and Cristina E. Cappa: Facultad de Ciencias Astronómicas y Geofísicas, Universidad Nacional de la Plata, Paseo del Bosque s/n, 1900, La Plata, Argentina.
Mónica Rubio: Departamento de Astronomía, Universidad de Chile, Chile (mrubio@das.uchile.cl).
Jura Borissova: Instituto de Física y Astronomía, Universidad de Valparaíso, Av. Gran Bretaña 1111, Playa Ancha, Casilla 5030, Chile.
Verónica Firpo: Departamento de Física y Astronomía, Universidad de La Serena, La Serena, Chile.
C.-H. López-Caraballo: Universidad Católica de Chile, Santiago, Chile.